

Divertor Impurity-Influx Monitor for ITER: Spectral Throughput Measurement on an Optical Prototype for the Upper Port and Optimization of Viewing Chords based on Computerized Tomography

Atsushi IWAMAE, Tatsuo SUGIE, Hiroaki OGAWA and Yoshinori KUSAMA

Fusion Research and Development Directorate, Japan Atomic Energy Agency, Naka, Ibaraki 311-0193, Japan

(Received 16 June 2009 / Accepted 14 July 2009)

We are developing a spectroscopic diagnostics system in ultraviolet and visible wavelength regions for monitoring ITER divertor plasmas. An equivalent-size prototype of the optical components for viewing upper port fan-array chords has been assembled as a system to measure spectral throughput, i.e., étendu. Collisional-radiative models for He I and C IV are used to estimate the emission line intensities of helium ash and carbon impurity ions in a divertor region of a burning plasma. The estimated line intensity of C IV, $\lambda 772.6$ nm, satisfies ITER requirements for the time resolution of measurement of T_i . A numerical simulation of the computerized tomographic technique for various pairs of viewing fan arrays has been applied to the divertor plasma region to reconstruct a two-dimensional distribution. The optimized pair of viewing fan arrays resolves a model distribution with a reasonable spatial resolution. We measure the reflectance of surfaces of carbon-fiber-composite and tungsten blocks, which make up the plasma-facing divertor target plates and the divertor dome. The reflectance of the surface of the tungsten divertor block is 23% at H_α ($\lambda 656.3$ nm). A sandblast-processed tungsten surface effectively reduces direct reflectance; the resultant reflectance is less than 0.7%.

© 2009 The Japan Society of Plasma Science and Nuclear Fusion Research

Keywords: divertor impurity-influx monitor, ITER, collisional-radiative model, computerized tomography, maximum entropy method, reflectance, tungsten, carbon-fiber-composite CFC

DOI: 10.1585/pfr.4.042

1. Introduction

ITER-oriented research has proceeded at the Japan Atomic Energy Agency (JAEA) to achieve the required specifications for plasma measurement [1]. JAEA has a procurement plan to supply a divertor impurity-influx monitor for ITER. Developments in schematic design and research on the divertor impurity-influx monitor have been presented [2–8]. Table 1 shows ITER specification requirements related to the divertor impurity-influx monitor for plasma measurement. The monitor measures the emission in a wide spectral range, from $\lambda 200$ nm to $\lambda 1000$ nm, along multiple lines of sight in the divertor region. The principal functions of the monitoring system are to identify impurity elements, measure concentrations and influxes [9, 10] of impurities, deuterium, and tritium for control, and obtain important parameters for optimization such as the energy of impurity elements (i.e., ion temperatures) and the ionization front position. The expected impurities are beryllium [11], carbon [12], and tungsten [13] originating from the first wall in the main chamber and from the inner and outer divertor target plates. Neon and other impurity gases injected into the plasma for radiation cooling in the divertor are also expected. It also monitors electron temperature

T_e and density n_e as well as the fuel ratio n_H/n_D or n_T/n_D of the divertor plasma. It provides supplementary information about the radiation power and profiles in the divertor and X-point/multi-faceted asymmetric radiation from the edge (MARFE) [14] regions, and also information about the densities of neutral atoms n_H , n_D , and n_T and molecules n_{H_2} , n_{D_2} , and n_{T_2} . The ITER vacuum vessel consists of eighteen port sections numbered from #01 to #18. The system is slated for installation in the upper #01, equatorial #01, and divertor #02 ports. Table 2 indicates its components, roles, designed spatial resolutions, and present status. Table 3 shows a proposal for spectrometers.

From the upper #01, equatorial #01, and divertor #02 ports, we observe the divertor plasma with a fan-array of viewing chords (see Figs. 1 and 2). Plasma emissions from the divertor region can be observed with 72 fan-array chords from the upper port #01 across the core plasma and with 72 chords from equatorial port #01. We propose observing the plasma with upper and lower fan-arrays from the gap between divertor cassettes in divertor port #02. The w-type divertor consists of central domes, inner and outer target plates, and baffles. The domes and baffles are made of tungsten (W) blocks. The divertor strike points are placed on a target plate made of carbon-fiber-composite (CFC) material. The optical design of the fan-array view-

author's e-mail: iwamae.atsushi@jaea.go.jp

Table 1 ITER specification requirements related to the divertor impurity-influx monitor for plasma measurement. (Quoted from Ref. [1]; copyright 2007 with permission from IAEA.)

Measurement	Parameter	Range	Time	Resolution		Accuracy
				Time	Space	
1. Impurity and D, T influx in the divertor	$\Gamma_{\text{Be}}, \Gamma_{\text{C}}, \Gamma_{\text{W}}$	$10^{17} - 10^{22}$ at s^{-1}	1 ms	50 mm	30%	
	$\Gamma_{\text{D}}, \Gamma_{\text{T}}$	$10^{19} - 10^{25}$ at s^{-1}	1 ms	50 mm	30%	
2. Divertor Helium density	n_{He}	$10^{17} - 10^{21}$ m^{-3}	1 ms	—	20%	
Fuel Ratio in the divertor	$n_{\text{T}}/n_{\text{D}}$	0.1 – 10	100 ms	integral	20%	
	$n_{\text{H}}/n_{\text{D}}$	0.01 – 0.1	100 ms	integral	20%	
3. Divertor electron parameters	n_{e}	$10^{19} - 10^{22}$ m^{-3}	1 ms	50 mm along leg, 3 mm across leg	20%	
	T_{e}	0.3 eV – 200 eV	1 ms	50 mm along leg, 3 mm across leg	20%	
4. Divertor ion temperature	T_{i}	0.3 eV – 200 eV	1 ms	50 mm along leg, 3 mm across leg	20%	
5. Divertor plasma flow	V_{p}	TBD– 10^5 ms	1 ms	100 mm along leg, 3 mm across leg	20%	
6. Divertor operational parameters	Position of the ionization front	0–TBD m	1 ms	100 mm	—	

Table 2 The divertor impurity-influx monitoring system.

Port	Mirror Optics system	Role	Spatial Resolution	Present status
Upper port #01	Front-end and Collection optics system	Two-dimensional measurement of divertor and x-point region	< 40 mm	An optical prototype is fabricated.
Equatorial port #01	Front-end and Collection optics system	(except near divertor target plates)	< 40 mm	Optical design has been completed.
Divertor port #02(g)	Upper and Lower Gap, (Relay) and Collection optical system	Observe divertor target plates	—	Optical design in process to fit the new divertor dome.
Divertor port #02(c)	Inside-Dome, (Relay) and Collection optics system	Observe divertor target plates	—	Optical design in process to fit the new divertor dome.

(c) Diagnostics access through the center of a cassette.

(g) Diagnostics access in a 20-mm gap between cassettes (see Fig. 2).

Table 3 Proposal for ITER divertor spectrometers with an observation wavelength range from $\lambda 200$ nm to $\lambda 1000$ nm.

Spectrometer	Location	Wavelength region	Time resolution	Aim
1. UV spectrometers	Behind the bio-shield: Port cell	$\lambda 200 - \lambda 450$ nm	10 ms	Impurity element monitoring and particle influx measurement in the UV region
2. Visible survey spectrometers	Diagnostic hall	$\lambda 400 - \lambda 1000$ nm	10 ms	Impurity element monitoring and particle influx measurement in the UV region
3. High-resolution spectrometers	Diagnostic hall	$\lambda 400 - \lambda 1000$ nm	100 ms	Ion temperature, particle energy distribution Tritium/deuterium/hydrogen density ratio from Balmer- α emissions
4. Filter spectrometers	Diagnostic hall	$\lambda 400 - \lambda 1000$ nm	1 ms	Two-dimensional measurement of particle influxes, the ionization front and helium density

ing chords for observing inner and outer target plates from the inside of the dome in the central divertor is in process.

The first walls are covered with beryllium. Helium ash atoms after D-T fusion reactions are pumped out at the divertor. The impurity influx Γ_{Be} , Γ_{C} , Γ_{W} , and Γ_{He} (Γ_{Ne} , Γ_{Ar} , Γ_{Xe} etc.) and the above parameters are monitored in the ultra-violet (UV), visible, and near infrared (IR). The collected emission from the divertor is divided and sent to three spectrometers: UV, visible survey, and high-resolution. High-resolution spectrometers measure line profiles and shifts and deduce the dynamics of impurity elements emitted from the divertor plates. The fuel influx in the divertor Γ_{D} and Γ_{T} which also helps in determining the fuel ratio from the intensity of the D_α and T_α emission lines, is measured using high-resolution spectrometers. The wavelength of the H_α , D_α and T_α emission lines are $\lambda 656.280$, $\lambda 656.104$ and $\lambda 656.045$ nm, respectively. Polarization separation measurement is necessary to select the π -light of the D_α and T_α emission lines [15,16]. Simultaneous measurements of both polarization components π and σ may indicate the emission location via Zeeman split spectral profiles [17–19]. The electron velocity distribution function may be determined by plasma polarization spectroscopy [20,21]. The ion temperatures in the divertor plasma are deduced from the Doppler broadening of the lithium-like C IV $\lambda 772.6$ nm line (C^{3+} , $n = 6 - 7$) [12]. The plasma parameters of electron temperature T_e and electron density n_e are derived from the ratio of the emission line intensity of He I when the ionizing plasma component is dominant. If the monitoring wavelengths of impurity emission lines and bremsstrahlung continuum and the wavelength bandwidths of the filters are determined, some of the optical fibers transmitting light from the collection optics system to visible survey spectrometers can be connected with filter spectrometers, which provide faster time resolution.

Reference [22] estimates the neutron flux and energy deposition in mirror materials and vacuum windows. The predicted neutron flux and the nuclear heat production of the first mirror, located about 1 m behind the first wall, are $1.2 \times 10^8 \text{ m}^{-2}\text{s}^{-1}$ and 20 kWm^{-3} , respectively. The radiation level has no effect on the molybdenum mirror surface at a neutron irradiation level of 1.4×10^8 neutrons m^{-2} [23]. Irradiation of low-energy deuterium ions on molybdenum and tungsten mirrors decreases the reflection; however, the decrease in reflectivity of the mirrors due to sintering without surface melting is less than 10% [24]. The nuclear heating power for stainless steel is 0.2 MW m^{-3} in the upper port. To remove the nuclear heat, water-cooling channels are bored into the mirror support structure. Heat load analysis has shown that the effect of thermal deformation is relatively low for the upper port optical components [4].

Here, we assembled the upper port optical components into a scale-size model viewing system. Its spectral light throughput, the étendue, was measured in the near UV, visible, and near IR regions. We examined the field

of view of sight chords of the prototype optical system. The two-dimensional spatial resolution was evaluated by means of the computerized tomography.

2. Scale-size Optical Prototype

2.1 Spectral throughput (étendue) of the upper port chords

Figure 1 shows the ray tracing of the viewing chords of the optical prototype used in the present experiment, which consists of 50 fan-array chords. The major and minor radii of the ITER plasma, R_p and a , are 6.2 m and 2.0 m, respectively. The plasma elongation is $\kappa = a/b = 1.85$. Thus, the length from the first mirror of the front-end optics to the divertor region is about 8 m. The 50 fan-array covers a 2-m divertor region along the poloidal direction.

Emission light from the divertor plasma is relayed through the front-end optical components. The front-end system consists of a plane molybdenum mirror (M1), an off-axis paraboloid molybdenum mirror (M2), and a plane aluminum mirror (M3), as shown in Fig. 1. Two Al-coated glass mirrors (M4 and M5) create a dog-leg for the light path. A Cassegrain telescope focuses the relayed divertor image onto a focal plane. A fifty-channel micro-lens array is set at the focal plane of the Cassegrain telescope. The array is placed to collect the light in the toroidal di-

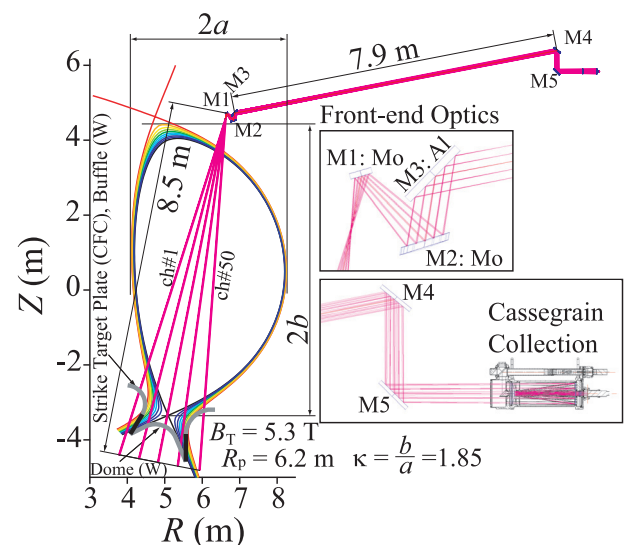


Fig. 1 Poloidal cross section of ITER. We have built a 50-channel fan-array of viewing chords for a prototype of the upper part of the divertor impurity-influx monitor for ITER. Magenta lines show ray tracing simulation of the fan-array viewing chords of the prototype. The length from the first mirror of the upper port to the divertor plasma is about 8 m. The 50-channel fan-array covers a poloidal region of approximately 2 m. The divertor dome and upper baffles of the inner and outer divertor plates will be made of tungsten (W) blocks. Carbon-fiber-composite (CFC) blocks will be used for strike points of the inner and outer divertor plates.

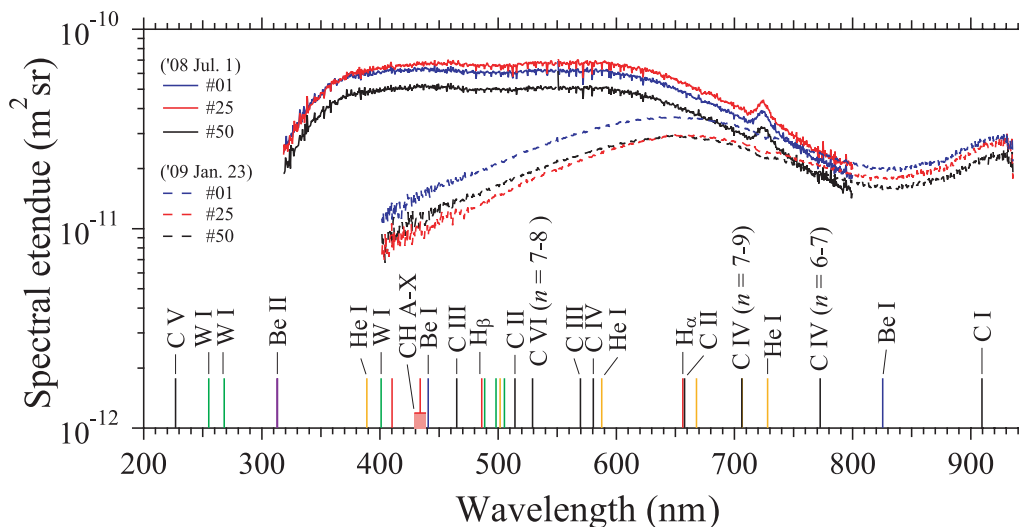


Fig. 3 The measured spectral light throughput coefficients (étendue) for the upper port prototype. The observed spectral étendue of three chords, #1, #25, and #50, is shown as an example. We re-measured the spectral étendue about seven months after the first measurement. The deterioration of the spectral étendue at shorter wavelengths is shown with dashed curves. Tarnished spots can be seen on the surface of the molybdenum mirrors. The deterioration of the off-axis paraboloid mirror (M2) is quite considerable. Expected emission lines from the divertor plasma are indicated by bars at the bottom of the graph.

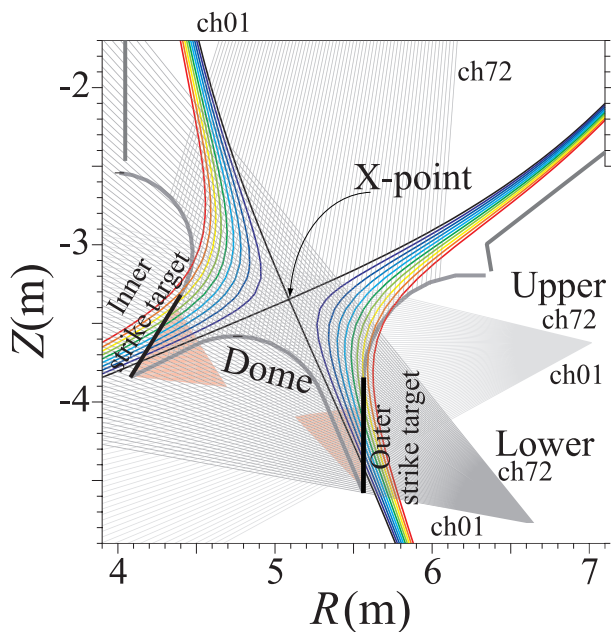


Fig. 2 Planned viewing fan-arrays from upper port #01 and from the 20-mm gap between divertor cassettes in divertor port #02. Two gap fan-arrays are located at the upper and lower levels of the divertor. The optical design of fan-array viewing chords from the inside of the dome to observe the inner and outer strike target plates is in process (red hatched viewing fields). The viewing chords from equatorial port #01 are not shown in this schematic drawing (see Table 2).

rection while maintaining the poloidal spatial resolution. It is made of synthetic silica and contains a biconvex lens with a thin-height of 250 μm, lens front and end surface

curvatures of $r = 3.3$ mm, and a lens thickness of 6.7 mm. Ten slab-type biconvex lenses are molded into one unit. Five units are bonded with a binding material. Each lens is coupled with an optical fiber with a core diameter of 200 μm. The fiber interval is 250 μm to fit the micro-lens array. FC-type connectors are attached to 2-m fiber cables on the output side, numbered from #1 to #50.

We measured the spectral light throughput coefficient (étendue) of the fifty chords of the optical prototype twice over a period of about seven months. Initially, a standard light source (xenon arc lamp) irradiated a Spectralon reflectance target plate at a distance of 0.50 m. The manufacturers provided its calibration values of spectral irradiance at $\lambda 200$ nm - $\lambda 800$ nm and reflectance of the target plate at $\lambda 250$ nm - $\lambda 2500$ nm. The target plate was placed in front of the first mirror (M1) at a distance of 300 mm. An FC-FC connector and a 20-m optical fiber cable (FC-SMA) transferred the collected light to a portable spectrometer (B&WTEK BTC112).

Figure 3 shows the measured spectral étendue of chords #1, #25, and #50 of the optical prototype plotted with solid curves. The spectral étendue of chords #1, #25, and #50 is almost constant from $\lambda 400$ to $\lambda 600$ nm at 6.2 , 6.8 , and 5.0×10^{-11} m² sr, respectively. For shorter wavelengths, below $\lambda 400$ nm, the spectral étendue rapidly decreased to $\sim 2 \times 10^{-11}$ m² sr at $\lambda 320$ nm. For longer wavelengths, above $\lambda 600$ nm, the spectral étendue gradually decreased to $\sim 2 \times 10^{-11}$ m² sr at $\lambda 800$ nm. The small peaks at $\lambda 723$ nm are pseudo-peaks of the xenon line from the light source.

Gray spots expanded gradually on the surface of the molybdenum mirrors. In particular, the surface of the off-axis paraboloid molybdenum mirror drastically deteri-

orated. The center of the plane molybdenum mirror was also tarnished. After about seven months, an integrating sphere (Labsphere USS-1200) was used to re-measure the spectral étendue. The light source was a tungsten-halogen lamp. Calibration values of the spectral radiance between $\lambda 300$ nm and $\lambda 1000$ nm were provided by the manufacturer.

Figure 3 depicts the results plotted with dashed curves for chords #1, #25, and #50. A gradual deterioration of the spectral étendue at shorter wavelengths is clearly seen. At $\lambda 400$ nm for chord #25, the étendue decreases to 6.8×10^{-12} m² sr, which is one order of magnitude lower than that measured the first time.

A molybdenum corner cube mirror stored in a desiccator for several years has kept a metallic mirror surface with no degradation in the same experimental room as the mirror showing oxidation. The experimental room is air-conditioned; however, the relative humidity exceeds 80% on some days in the rainy season. We suspect that the high humidity in the air and some treatment during surface polishing might have caused the surface oxidation, leading its surface to gradually deteriorate. A storage case for desiccation or vacuum pumping for storing the optical head is necessary to maintain the reflectivity of the molybdenum mirrors on a par with a newly produced version.

The spectral étendue around $\lambda 700$ nm and $\lambda 800$ nm is unaffected by surface deterioration. Its value registers a minimum of $\sim 1.6 \times 10^{-11}$ m² sr at around $\lambda 830$ nm. The spectral étendue in the wavelength region above $\lambda 934$ nm is too low to measure in this experiment, at least one order of magnitude lower than $\sim 2 \times 10^{-11}$ m² sr. The light-absorption in this wavelength region is enhanced by hydroxyl (-OH) bonds doped in the optical fiber to increase UV transmittance.

2.2 Spatial resolution of the viewing field

A bright white light from a fiber-coupled Xe lamp was inserted at each end of optical fiber cables connected to the Cassegrain telescope. The image was projected on a white reflectance target plate 8.5 m from the first mirror. The images on the target plate were taken with a digital single-lens reflection camera (Nikon D60 with a zoom lens 18-55 mm F3.5-5.6G). We calibrated the scale of the digital camera image by taking a picture of a cross-sectional paper under the same focal conditions.

Figure 4 shows an example of the projected image of the micro-lens coupled optical-fibers. Intensities of 90% are recorded in the width from 27 mm to 34 mm along the poloidal direction. These values satisfy the ITER requirement of a 50-mm resolution. The surface of lens #50 is rather rough, so the spectral étendue of this chord is the lowest of the 50 chords. The intensity of the 5% overlap with the neighboring chord can be seen on the cross sections of lens #25 and #26.

The curvature and thickness of the biconvex micro-

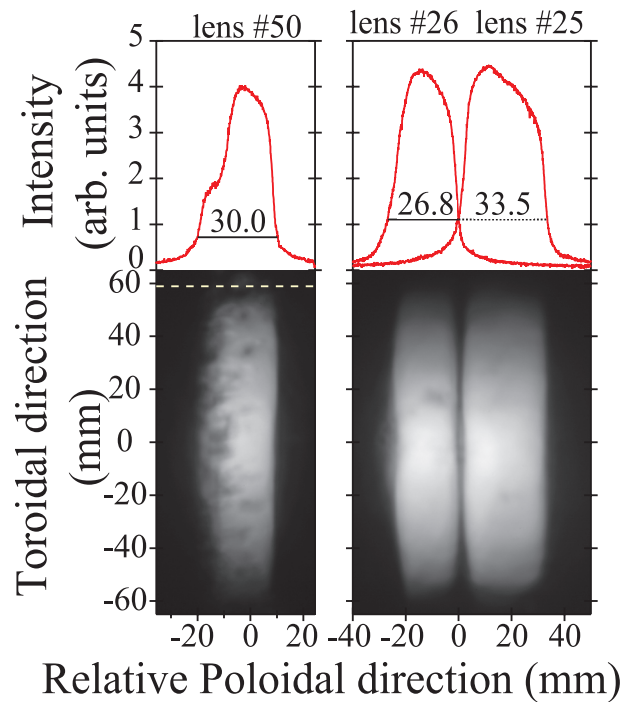


Fig. 4 Photographs showing two-dimensional intensity distribution of the micro-lenses of chords #25, #26, and #50. The cross section (red curve) at the center along the poloidal direction appears above each of the photographs. Widths of the lens images (27 mm to 34 mm) in the poloidal direction are less than 50 mm. This degree of spatial-resolution in the poloidal direction satisfies ITER requirements. The image of chords #25 and #26 is digitally synthesized from separate images of each chord.

lens used in the present experiment are $r = 3.3$ mm and $t = 6.7$ mm, respectively, which are feasible for manufacturing. If the ideal micro-lens of $r = 2.45$ mm and $t = 7.45$ mm becomes feasible in the future, the light collection efficiency will increase about three times, which is calculated by a ray tracing simulation code. A Herschelian telescope is also proposed as a collection optics device to increase the light collection efficiency by a factor of 1.3.

For the planned divertor impurity-influx monitor for ITER, spectral emissions in the UV region between $\lambda 200$ nm and $\lambda 450$ nm will be monitored with the nearby UV spectrometers located just behind the bio-shield in the port cell. Cassegrain collection optical components and UV spectrometers will be connected by a few meters of optical fiber to avoid attenuation of the UV light intensity. Emissions in the visible region will be transferred to a diagnostics hall by long (of the order of a hundred meters) optical fiber cables. In the diagnostics hall, spectral emissions are recorded by means of visible survey spectrometers, high-resolution spectrometers, and filter spectrometers (see Table 3).

3. Emission Intensity Estimation of Impurities

The B2-EIRENE code package [25] simulates the neutral atom and ion distribution in the ITER scrape-off layer and divertor private plasma region. The calculated condition is as follows: $I_p = 15$ MA, $B_T = 5.3$ T, $P_{\text{fusion}} = 600$ MW, ($Q = 20, P_{\text{NBI}} = 30$ MW), a flux of deuterium from the core of $9 \times 10^{21} \text{ s}^{-1}$, and a gas-puff rate of $1.4 \times 10^{23} \text{ s}^{-1}$. Simulation results are supplied by Dr. Kukushkin [26]. Figure 5 shows the B2-EIRENE simulation results, which give the two-dimensional (a) T_e and (b) n_e distribution, and (c) helium atom and (d) ion density distribution, and various ion stages of carbon ion distribution. Densities of C^{3+} and C^{4+} are depicted in Fig. 5 (e) and (f), respectively.

The spontaneous transition probability from upper state k to lower state i , A_{ki} , is related to the total intensity

I_{ki} in photon numbers by

$$I_{ki} = \frac{1}{4\pi} A_{ki} n(k), \quad (1)$$

where $n(k)$ is the population density of state k . The level population densities $n(k)$ are calculated based on collisional-radiative (CR) models. The emissivity of impurity lines from the ITER divertor plasma is estimated by means of CR models on He I [27, 28] and C IV [12], on the condition of the given plasma parameters (Fig. 5).

Figure 6 shows an example of the two-dimensional emissivity distribution of the He I $\lambda 587.6 \text{ nm}$ ($2^3\text{P} - 3^3\text{D}$) line: the ionizing component generated from a helium ground state (a) and the recombining component from He^+ ions (b) are separately plotted. For the ionizing component, high emissivity over ($1 \times 10^{19} \text{ ph s}^{-1} \text{ m}^{-3} \text{ sr}^{-1}$) is observed around the inner and outer divertor leg strike points (the orange regions shown in Fig. 6 (a)). For the recombining plasma component, the highest emissivity over ($1 \times 10^{20} \text{ ph s}^{-1} \text{ m}^{-3} \text{ sr}^{-1}$) is observed in front of the inner divertor-leg strike point (the red region in Fig. 6 (b)). In front of the outer divertor-leg strike point, the emissivity is between $1 \times 10^{19} \text{ ph s}^{-1} \text{ m}^{-3} \text{ sr}^{-1}$ and $1 \times 10^{20} \text{ ph s}^{-1} \text{ m}^{-3} \text{ sr}^{-1}$ (shown in orange). These tendencies in emissivity distribution can be observed for other transitions of the He I $n = 3$ to $n = 2$ transition manifold.

These emission lines of impurities are observed with the fan-array chord from the upper port (see Fig. 1). Figure 7 shows the line-of-sight integrated radiance of the He I emission line $\lambda 587.6 \text{ nm}$. For the upper port view, emission lines in front of the strike points are eclipsed by the diver-

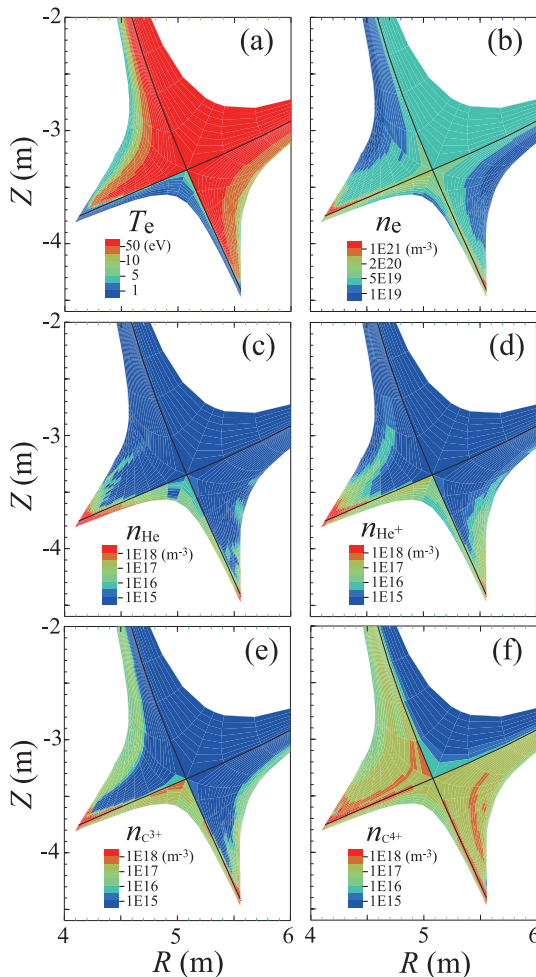


Fig. 5 Two-dimensional distributions of plasma parameters in the divertor plasma, based on B2-EIRENE numerical simulation: (a) electron temperature T_e , (b) electron density n_e , (c) helium atom density n_{He} , (d) helium ion density n_{He^+} , (e) C^{3+} ion density $n_{\text{C}^{3+}}$, and (f) C^{4+} ion density $n_{\text{C}^{4+}}$.

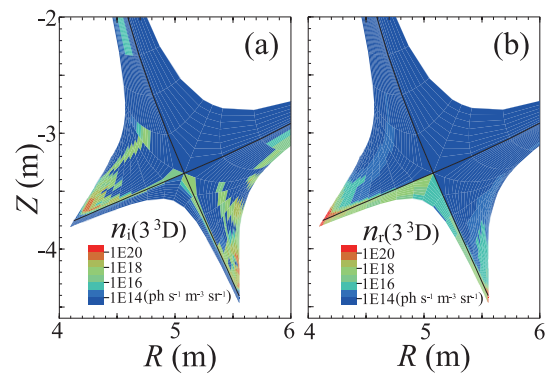


Fig. 6 Two-dimensional distributions of the emissivity in the units of photons $\text{s}^{-1} \text{ m}^{-3} \text{ sr}^{-1}$ of He I $\lambda 587.6 \text{ nm}$ ($2^3\text{P} - 3^3\text{D}$) for (a) the ionizing plasma component excited from the ground state of He atoms: High emissivity (more than $1 \times 10^{19} \text{ ph s}^{-1} \text{ m}^{-3} \text{ sr}^{-1}$) is observed around the inner and outer divertor leg strike points (orange region). (b) The recombining plasma component produced from He^+ ions. The highest emissivity (more than $1 \times 10^{20} \text{ ph s}^{-1} \text{ m}^{-3} \text{ sr}^{-1}$) is observed at the inner divertor leg strike point (red region). At the outer strike point, the emissivity ranges between $1 \times 10^{19} \text{ ph s}^{-1} \text{ m}^{-3} \text{ sr}^{-1}$ and $1 \times 10^{20} \text{ ph s}^{-1} \text{ m}^{-3} \text{ sr}^{-1}$ (orange region).

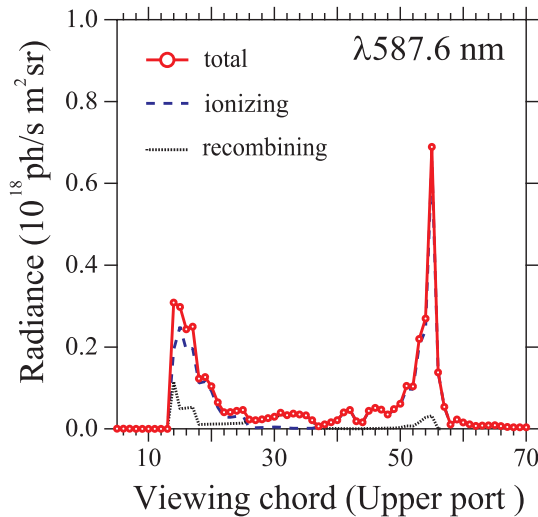


Fig. 7 Chord integrated emission intensity of He I $\lambda 587.6$ nm ($2^3P - 3^3D$). The ionizing plasma component is dominant for the upper port viewing chords.

tor baffle, as shown in Fig. 2. The contribution from the ionizing and recombining plasma components [29] is indicated with dashed and dotted curved lines, respectively. Total intensity is plotted with a solid curve and circles. The ionizing plasma component is mostly dominant. Near the strike points in front of the inner and outer divertor targets, the plasma temperature is low ($T_e < 1$ eV) and the density is rather high ($n_e > 1 \times 10^{21} \text{ m}^{-3}$), as shown in Fig. 5 (a) and (b), respectively, leading to speculation that a detached plasma may have formed. The inner and outer divertor target plates will be observed from inside the dome as shown in Fig. 2. Recently, the divertor dome design has been changed. Revision of the internal design of the optical system to fit the changed dome is now underway.

All the helium emission lines from $n = 3$ to $n = 2$ transitions are shown in Fig. 8 in logarithmic plots. Figure 8 (a) shows singlet transitions: $\lambda 501.6$ nm ($2^1S - 3^1P$), $\lambda 667.8$ nm ($2^1P - 3^1D$), and $\lambda 728.1$ nm ($2^1P - 3^1S$), and Fig. 8 (b) shows triplet transitions: $\lambda 388.9$ nm ($2^3S - 3^3P$), $\lambda 587.6$ nm ($2^3P - 3^3D$), and $\lambda 706.5$ nm ($2^3P - 3^3S$).

The maximum and minimum estimated chord-integrated signal intensities in photo-electrons per second for He I and C IV are estimated in Tables 4 and 5, respectively. For He I, because of the low photon radiation around the X-point (see Fig. 6), the lowest estimated signal intensity is 227 photoelectrons per second for the $\lambda 728.1$ nm line (see Table 4). The signal-to-noise ratio is about 25. The line intensity ratios of $I(667.8 \text{ nm})/I(728.1 \text{ nm})$ and $I(728.1 \text{ nm})/I(706.5 \text{ nm})$ are often used as indicators of n_e and T_e , respectively, on the condition that the population production is dominant from the ionizing plasma component. To obtain the line-averaged n_e and T_e distributions by means of helium ash, without helium gas puffing at the divertor plasma, we need an exposure time of a few seconds

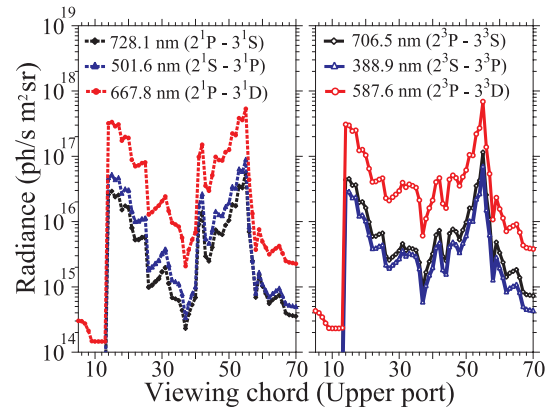


Fig. 8 Chord integrated emission intensity of He I $n = 2 - 3$ manifold (a) singlet transitions and (b) triplet transitions.

with the present optical system.

Figure 9 and Table 5 show the chord-integrated radiance of the $\lambda 580.5$ nm (580.151 nm, 581.214 nm: $3s^2S_{1/2} - 3p^2P_{1/2,3/2}$) and $\lambda 772.6$ nm ($n = 6 - 7$) transitions in C IV (C^{3+}) ions and estimated minimum and maximum photoelectrons we observe by a spectrometer with a CCD detector, respectively. The radiance of the $\lambda 772.6$ nm ($n = 6 - 7$) emission line is rather high; its highest value is above $10^{19} \text{ ph s}^{-1} \text{ m}^{-2} \text{ sr}^{-1}$. It is expected that with a high-resolution spectrometer, spectral profiles of the $\lambda 772.6$ nm line provide T_i at a fast time resolution. This line is dominantly populated from the recombining plasma component from C^{4+} ions. The line $\lambda 580.49$ nm is important for the branching ratio to $\lambda 31.24$ nm ($2s,^2S_{1/2} - 3p^2P_{1/2,3/2}$) in vacuum UV measurements.

From the upper port, the chords observe the divertor region through the core plasma. The intensity of bremsstrahlung is estimated to be on the order of $10^{17} \text{ ph s}^{-1} \text{ m}^{-2} \text{ sr}^{-1} \text{ nm}^{-1}$ at an electron density of $1 \times 10^{20} \text{ m}^{-3}$ for the chord through the center of the core. If we use a spectrometer, the bremsstrahlung continuum component and the divertor impurity emission lines are easily distinguishable. For filter spectrometers, filters for monitoring the bremsstrahlung continuum are needed in addition to the emission-line filters. For He I and C IV, emission contributions from the upper common flux region are negligible based on CR model calculations.

The absolute intensity calibration is important for population density estimation. Test results of the in situ calibration method using a micro-retro-reflector array plate located in the front-end optical system are reported separately [2].

4. Computerized Tomography

The divertor consists of 54 divertor cassettes, i.e., 3 cassettes for each port. In our former design, two fan-array chords emanate from the gaps between divertor cassettes in the lower outer region on both sides of the cassette. We

Table 4 Estimated photoelectrons per second for He I emission lines with the CR model.[□]

Transition	2 ¹ S – 3 ¹ P		2 ¹ P – 3 ¹ D		2 ¹ P – 3 ¹ S	
Line (nm)	λ501.6		λ667.8		λ728.1	
Int. min., max. (10 ¹⁶ ph/s m ² sr)	0.0334	8.82	0.208	53.4	0.0231	5.61
Spec. étendue (10 ⁻¹¹ m ² sr)	6.59		4.94		3.49	
Triple-branched	0.152		0.152		0.152	
Transmission ^{† ‡}	0.813		0.827		0.828 [†]	
Spectrometer effi. [×]	0.5		0.5		0.5	
Grating effi. [*]	0.786		0.648		0.548	
Detector effi. ⁺	0.884		0.908		0.817	
Ph-elec/s min, max [°]	945	250 000	3 800	976 000	227	55 100

Transition	2 ³ S – 3 ³ P		2 ³ P – 3 ³ D		2 ³ P – 3 ³ S	
Line (nm)	λ388.9		λ587.6		λ706.5	
Int. min., max. (10 ¹⁶ ph/s m ² sr)	0.0577	6.92	0.608	68.9	0.0920	11.5
Spec. étendue (10 ⁻¹¹ m ² sr)	6.13		6.28		3.97	
Triple-branched	0.152		0.152		0.152	
Transmission ^{† ‡}	0.982 [†]		0.762		0.814 [‡]	
Spectrometer effi. [×]	0.5		0.5		0.5	
Grating effi. [*]	0.452		0.730		0.583	
Detector effi. ⁺	0.375		0.937		0.864	
Ph-elec/s min, max [°]	328	39 400	15 100	1 710 000	1 425	178 000

[□] Assumptions: For visible wavelengths, a 100-meter, OH-doped optical fiber transfers the light from the collection optics to a diagnostics room. [†]For UV wavelengths, spectrometers are placed near the collection optics behind a bio-shield and connected with a 2-m, OH-doped optical-fiber bundle. [‡]For the near IR region above 700 nm, a 100-meter Ge-doped optical fiber bundle is used to avoid OH-band absorption. [×]Spectrometer efficiency depends on the slit width, the spectral reflectivity of the mirrors used and the light-coupling efficiency aberration correction of optical components placed in front of the entrance slit. Here, we assumed it is constant. ^{*}Efficiency curve of a grating with 1200 grooves/mm and 500 nm blaze wavelength. Input light is assumed to be unpolarized. ⁺The quantum efficiency of a CCD detector (ANDOR DU971N-UVB) is used as an example. [°]Dark electrons are estimated to be 9.1 electrons s⁻¹ at a detector temperature of -50°C. The area of 13 × 10-(16×16) μm²-pixels is assumed for a 200 μm core diameter of the optical fiber as the height and a 20 μm-slit width for the line profile with a background signal.

have changed this design by moving one of the two gap chords to a higher position on the same side of the divertor cassette in divertor port #02. The plasma is measured from the outer region through a gap of 20 mm between the divertor cassettes, as shown in Fig. 2, which shows the two gap fan-arrays of the upper and lower viewing chords.

To measure the ionization front at the divertor legs, a 100-mm spatial resolution is required for spectroscopic measurement, as shown in Table 1. The viewing chords for the inner and outer strike points along the divertor legs at the target plates are installed in the divertor dome. The

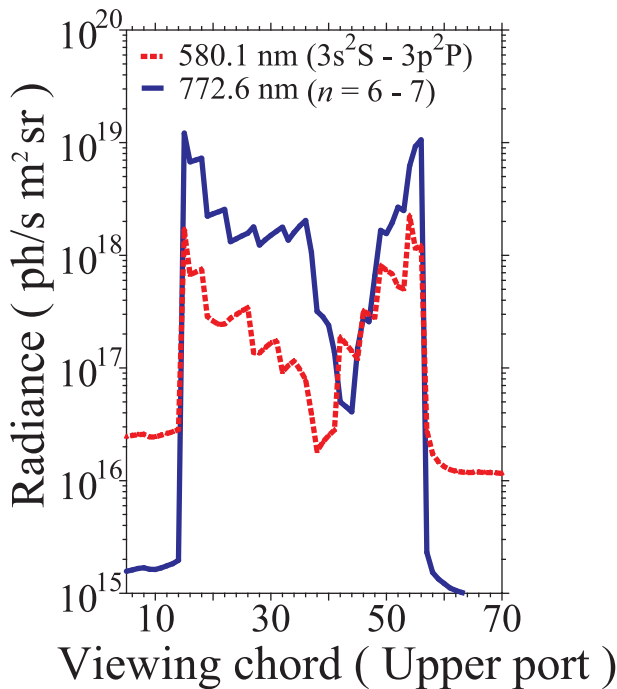
optical component box and the inner dome optical components that will fit into the new divertor dome are currently being designed.

In a CT simulation, a model distribution of the emission intensity, as shown in Fig. 10(a), is located at the X point with a full-width at half-maximum (FWHM) of 100 mm. Fig. 10(a)–(e) shows the CT reconstructed images. The maximum entropy method (MEM) [30] is applied to reconstruct a two-dimensional intensity distribution based on the integrated signal intensity. The element f_k of the image vector f is observed with the m -th obser-

Table 5 Estimated photoelectrons per second for C IV emission lines with the CR model.

Transition	$3s^2S_{1/2} - 3p^2P_{1/2,3/2}$		$n = 6 - 7$	
Line (nm)	$\lambda 580.49$ (580.151, 580.214)		$\lambda 772.6$	
Int. min., max. (10^{16} ph/s m^2 sr)	1.682	224.7	4.061	1219.1
Spec. étendue (10^{-11} m^2 sr)	6.81		2.43	
Triply-branched	0.152		0.152	
Transmission [‡]	0.788		0.857 [‡]	
Spectrometer effi. [×]	0.5		0.5	
Grating effi. [*]	0.735		0.508	
Detector effi. ⁺	0.940		0.720	
Ph-elec/s min, max [°]	47 400	6 330 000	26 600	7 050 000

The superscript symbols [‡], [×], ^{*}, ⁺, and [°] are the same as in Table 4.


 Fig. 9 Chord-integrated emission intensity from C IV (C^{3+}) ions.

vation chord. The signal intensity g_m of the m -th detector can be written as

$$\sum_{k=1}^K h_{mk} f_k = g_m, \quad (2)$$

where h_{mk} is the contribution from the image element f_k to the signal intensity g_m . We define h_{mk} as the length of the chord across the image element of f_k . We use the evaluation function

$$P(f) = \sum_{k=1}^K f_k \ln f_k. \quad (3)$$

The Lagrange function $\Lambda_\gamma(f)$ is minimized with an iterative solution technique.

The MEM code used here was originally developed for the divertor measurement of JT-60U plasma [31–33]. We modified the code to the ITER divertor configuration and the divertor impurity-influx monitor.

Currently, the code has an operational restriction: only two fan-array viewing chords are considered for the purpose of CT reconstruction. When we use the signal intensities for CT from the upper and equatorial chords in the port #01 section, the reconstructed image shown in Fig. 10(b) is elongated by a factor of four, compared to the original along the angle bisect of the upper and equatorial viewing chords. Using both the chords in the divertor gap in divertor port #02, the CT-reconstructed image is shown in Fig. 10(c), which is elongated in the horizontal direction by a factor of four. Assuming toroidal symmetry of the divertor plasma, as observed from neighboring ports #01 and #02, the signal intensities from both the upper port and the proposed gap fan-array chords can be used to create CT reconstruction images. The resulting CT images are shown in Fig. 10(d) and (e). For Fig. 10(d), we use the upper port chords and the lower gap fan-array. For Fig. 10(e), we use the upper port chords and the upper gap fan-array. With the upper port and the lower gap fan-array from the divertor port, the image is elongated vertically by a factor of two. The pair from the upper port and the upper gap fan-array from the divertor port give reasonable reconstructed images. The reconstructed peak shape is almost identical to the originals. With a pairing of the upper port and the upper gap fan-array, we are able to meet the ITER requirements for the spatial resolution of the ionization front. Note, how-

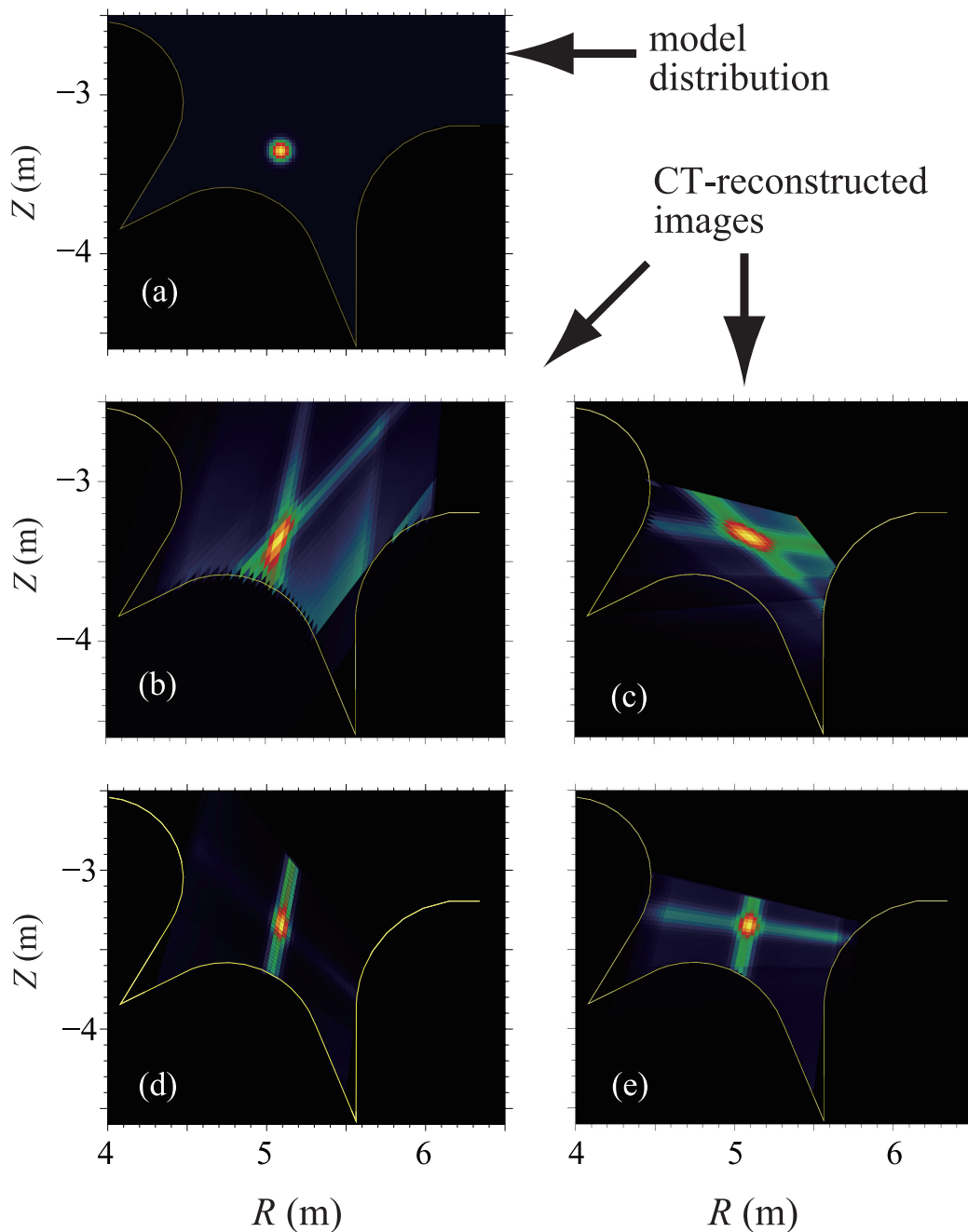


Fig. 10 Computerized tomographic simulation: (a) The model of the intensity distribution of a 100-mm FWHM Gaussian. Reconstructed images: (b) The upper and equatorial chords in ports #01 are used for the reconstruction, (c) Upper and lower gap fan-arrays in divertor port #02 are used for the reconstruction, (d) The upper port chord and lower gap fan-array, and (e) the upper port and upper gap fan-array are used for reconstruction with toroidal symmetry assumed.

ever, that artificially low intensity of base signals is generated in the CT-reconstructed images in a manner that may, for example, form a cross shape, as shown in Fig. 10 (e).

5. Reflectance of Divertor Blocks

The direct reflection of the bright light sources near the surface of the divertor materials (W and CFC) may affect the line-integrated intensity. We measured the spectral reflectance ($\lambda 200 \text{ nm} - \lambda 1100 \text{ nm}$) of W and CFC sam-

ple blocks provided by our divertor group. Measurements were performed using a spectrophotometer (Jasco V-570) with a single reflection attachment (SLM-468). The roughness of the W plasma-facing surface was less than $R_a = 3.2 \mu\text{m}$. A monochromatic spectral light-ray was inserted at six degrees to normal relative to the surface. The reflectance of a sandblasted W plate was also measured, because it was expected to exhibit reduced direct reflection.

Figure 11 shows the reflectance of the plasma-facing surface materials, W and CFC. The reflectance of the same

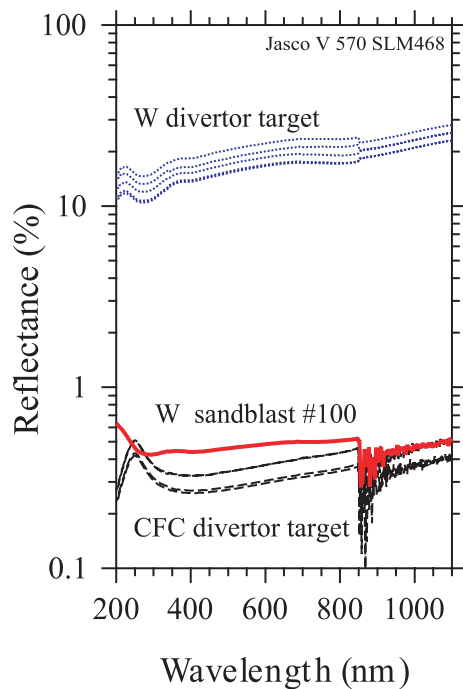


Fig. 11 Reflectance of the divertor blocks of tungsten (W: dotted lines) and carbon-fiber composite (CFC: dashed lines). The solid curve shows the reflectance of the sandblast-processed W surface. The detector for reflected light changes from a photo-multiplier to a PbS photodetector for wavelengths over 832 nm.

surface of both W and CFC is anisotropic relative to the direction of the block because of the circular milling grooves on the W surface and the laminated carbon-fiber sheets.

At the H_{α} wavelength of 656.3 nm, direct reflection of the W surface ranges from 17 to 23%. The direct reflection of the CFC surface is lower than that of W; the value ranges between 0.3 and 0.4%. The sandblasted W surface has the highest level of direct reflectance (0.7%) at 200 nm, is down to 0.4% at 275 nm, and is almost constant around 0.5%, gradually increasing with the wavelength. However, surface conditions drastically change due to the massive thermal heat load, erosion, and deposition. Prototype divertor targets made of CFC and W blocks with cooling pipes of CuCrZr have been constructed by the Blanket Technology group in JAEA. A qualification prototype of the divertor plate was sent to the Russian Federation to test the heat load with an electron beam. The post-test qualification prototype has since been returned. Recrystallization on the W surface is observed on some of the blocks. The surface of the recrystallized W looks white. Deposition of carbon is observed on a portion of the surfaces of W blocks. In this case, the surface is black. We plan to detailed measurements of the surface conditions of the heat-loaded W and CFC sample tiles.

Acknowledgments

The authors are grateful to Dr. S. Suzuki in the Blanket Technology group for supplying us with samples of the divertor blocks. One of the authors (A. I.) wishes to thank Mr. T. Tollefson for his careful reading of the manuscript.

- [1] A.J.H. Donné *et al.*, Nucl. Fusion **47**, S337 (2007).
- [2] H. Ogawa *et al.*, will appear in Nucl. Fusion. *Proceedings of IAEA conference IT-p6-23* (2009).
- [3] T. Sugie *et al.*, *Burning Plasma Diagnostics* ed. G. Gorini *et al.* (AIP, 2008) p.218.
- [4] H. Ogawa *et al.*, Plasma Fusion Res. **2**, S1054 (2007).
- [5] H. Ogawa *et al.*, *Design of Impurity Influx Monitor (Divertor) for ITER* JAEA-Tech. 2006-015 (2006). <http://jolissrch-inter.tokai-sc.jaea.go.jp/pdfdata/JAEA-Technology-2006-015.pdf>
- [6] T. Sugie *et al.*, J. Plasma Fusion Res. **79**, 1051 (2003).
- [7] T. Sugie *et al.*, *Design of Divertor Impurity Monitoring System for ITER (II)* JAERI-Tech 98-047 (1998). <http://jolissrch-inter.tokai-sc.jaea.go.jp/pdfdata/JAERI-Tech-98-047.pdf>
- [8] T. Sugie *et al.*, *Design of Divertor Impurity Monitoring System for ITER* JAERI-Tech 96-055 (1996).
- [9] K.H. Behringer, J. Nucl. Mater. **145-147**, 145 (1987).
- [10] N.J. Peacock, Astrophys. Space Sci. **237**, 341 (1996).
- [11] H.P. Summers *et al.*, Plasma Phys. Control. Fusion **34**, 325 (1992).
- [12] T. Nakano *et al.*, J. Plasma Fusion Res. **80**, 500 (2004).
- [13] I. Beigman *et al.*, Plasma Phys. Control. Fusion **49**, 1833 (2007).
- [14] B. Lipschultz *et al.*, Nucl. Fusion **24**, 977 (1984).
- [15] C.H. Skinner *et al.*, Nucl. Fusion **35**, 143 (1995).
- [16] C.H. Skinner *et al.*, J. Nucl. Mater. **241-243**, 887 (1997).
- [17] T. Shikama *et al.*, Phys. Plasmas **11**, 47011 (2004).
- [18] A. Iwamae *et al.*, Phys. Plasmas **12**, 042501 (2005).
- [19] A. Iwamae *et al.*, Phys. Plasmas **14**, 042504 (2007).
- [20] A. Iwamae *et al.*, Plasma Phys. Control. Fusion **47**, L41 (2005).
- [21] T. Fujimoto and A. Iwamae Eds., *Plasma Polarization Spectroscopy* (Springer, Berlin Heidelberg, 2008).
- [22] H. Iida *et al.*, *Nuclear Analysis Report G 73 DDD 2 W 0.2* (2004).
- [23] T. Nishitani *et al.*, Fusion Eng. Des. **42**, 443 (1998).
- [24] T. Sugie *et al.*, J. Nucl. Mater. **329-333**, 1481 (2004).
- [25] R. Schneider *et al.*, J. Nucl. Mater. **266-269**, 175 (1999).
- [26] V. Kotov, D. Reiter and A. S. Kukushkin, *Numerical study of the ITER divertor plasma with the B2-EIRENE code package* (Jülich 2007). http://www.eirene.de/kotov_solps42_report.pdf and *private communication*.
- [27] M. Goto and T. Fujimoto, *Collisional-radiative Model for Neutral Helium in Plasma: Excitation Cross Section and Singlet-triplet Wavefunction Mixing* NIFS-DATA-043 (1997). <http://www.nifs.ac.jp/report/NIFS-DATA-043.pdf>
- [28] M. Goto, JQSRT **76**, 331 (2003).
- [29] T. Fujimoto, *Plasma Spectroscopy* (Oxford University Press, Oxford, 2004).
- [30] N. Iwama and S. Ohdachi, J. Plasma Fusion Res. **82**, 399 (2006). [in Japanese]
- [31] K. Fujimoto *et al.*, Fusion Sci. Technol. **51**, 2T, 247 (2007).
- [32] K. Fujimoto *et al.*, Plasma Fusion Res. **2**, S1121 (2007).
- [33] K. Fujimoto *et al.*, Plasma Fusion Res. **4**, 025 (2009).